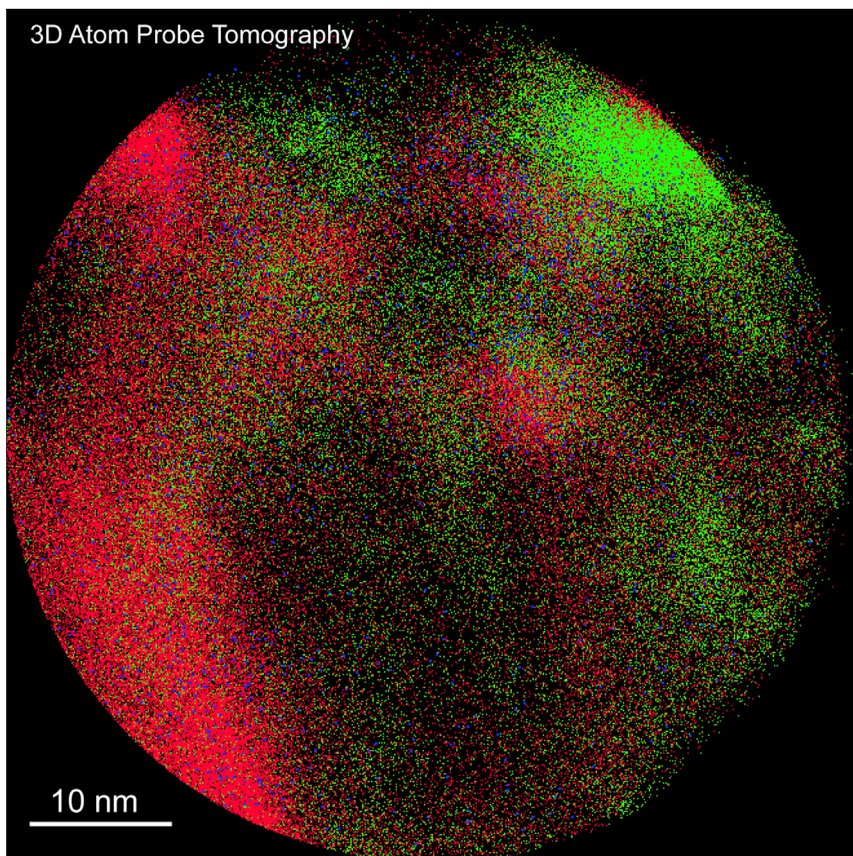


Article

Transition-Metal Single Atoms in a Graphene Shell as Active Centers for Highly Efficient Artificial Photosynthesis



State-of-the-art three-dimensional atom probe tomography provides direct evidence of Ni single atoms coordinated in graphene vacancies for highly selective CO₂ reduction to CO and suppressed hydrogen evolution in water.

Kun Jiang, Samira Siahrostami,
Austin J. Akey, ..., Jens K.
Nørskov, Yi Cui, Haotian Wang
hwang@rowland.harvard.edu

HIGHLIGHTS

Single Ni atoms coordinated in graphene exhibit superb catalytic CO₂RR performance

Atomic-resolution 3D APT provides direct identification of single Ni atoms

DFT simulations suggest that the tuning of electronic structure favors CO₂RR over HER

Article

Transition-Metal Single Atoms in a Graphene Shell as Active Centers for Highly Efficient Artificial Photosynthesis

Kun Jiang,^{1,11} Samira Siahrostami,^{2,11} Austin J. Akey,³ Yanbin Li,⁴ Zhiyi Lu,⁴ Judith Lattimer,⁵ Yongfeng Hu,⁶ Chris Stokes,¹ Mahesh Gangishetty,¹ Guangxu Chen,⁴ Yawei Zhou,⁷ Winfield Hill,¹ Wen-Bin Cai,⁷ David Bell,^{3,8} Karen Chan,⁹ Jens K. Nørskov,^{2,9} Yi Cui,^{3,10} and Haotian Wang^{1,12,*}

SUMMARY

Utilizing solar energy to fix CO₂ with water into chemical fuels and oxygen, a mimic process of photosynthesis in nature, is becoming increasingly important but still challenged by low selectivity and activity, especially in CO₂ electrocatalytic reduction. Here, we report transition-metal atoms coordinated in a graphene shell as active centers for aqueous CO₂ reduction to CO with high faradic efficiencies over 90% under significant currents up to ~60 mA/mg. We employed three-dimensional atom probe tomography to directly identify the single Ni atomic sites in graphene vacancies. Theoretical simulations suggest that compared with metallic Ni, the Ni atomic sites present different electronic structures that facilitate CO₂-to-CO conversion and suppress the competing hydrogen evolution reaction dramatically. Coupled with Li⁺-tuned Co₃O₄ oxygen evolution catalyst and powered by a triple-junction solar cell, our artificial photosynthesis system achieves a peak solar-to-CO efficiency of 12.7% by using earth-abundant transition-metal electrocatalysts in a pH-equal system.

INTRODUCTION

Effectively converting clean solar energy into carbon fuels via electrocatalytic carbon dioxide (CO₂) reduction and water oxidation, a mimic process of photosynthesis in nature, can potentially play a critical role in sustaining the global energy demands and in preventing further CO₂ emissions.^{1–6} However, this practical application is currently challenged by the low activity and selectivity of the CO₂ reduction reaction (CO₂RR) because of the high kinetic barriers and competition with the hydrogen evolution reaction (HER) in aqueous media.^{7–9} Strategies, including exploring novel catalysts^{8,9} or using non-aqueous electrolyte such as ionic liquid,^{10–12} have been extensively studied to reduce reaction barriers or suppress HER. Highly selective CO₂ reduction requires catalysts to have specific electronic structures that could facilitate the CO₂ activation process and also properly bind reaction intermediates, not too strong or too weak.¹³ A representative example is a transition-metal (TM) catalyst such as Au, which has been demonstrated to convert CO₂ to carbon monoxide (CO) with high selectivity,^{14–16} whereas Pt, with only one d-band electron less, generates H₂ exclusively and can be easily poisoned by CO.^{17,18} Other earth-abundant TMs such as Fe, Co, and Ni are rarely studied as CO₂ to CO catalysts, mainly because of their good HER activities as well as the strong bonding between CO and the metal surfaces.^{17–21} Therefore, how to effectively tune the catalytic electronic properties plays a critical role in searching for active CO₂RR catalysts.

The Bigger Picture

Using clean electricity to reduce CO₂ to chemicals or fuels is becoming increasingly important to renewable energy applications and environmental protection. The challenge comes from the strong competition with the hydrogen evolution reaction in aqueous solutions, especially for those earth-abundant transition metals such as Ni, which dramatically lowers the CO₂ reduction selectivity. Isolating the transition-metal single atoms into a graphene matrix can significantly tune their catalytic behaviors to favor the CO₂-to-CO reduction pathway, reaching a high CO selectivity of more than 90%. This work creates an important platform in designing active and low-cost CO₂ reduction catalysts with high selectivity toward fuels, opening up great opportunities for both technological applications in renewable energies and fundamental mechanism studies in catalysis.

Different methods, such as metal oxidation and metal alloying, have been demonstrated to be successful in engineering TM electronic states for improved CO₂RR activities.^{7,8,16,22–24} However, these engineering processes on TM catalysts usually result in complicated atomic structures and coordination, making it difficult to study and understand the possible catalytic active sites. Instead, introducing TM atoms into a well-established material matrix could open up great opportunities to (1) tune the electronic properties of TMs as CO₂RR active sites and (2) at the same time maintain relatively simple atomic coordination for fundamental mechanism studies.^{9,25} In addition, those TM atoms trapped in a confined environment cannot be easily moved around during catalysis, which prevents the nucleation or reconstructions of surface atoms observed in many cases.^{26–29} Graphene layers are of particular interest as host for TM atoms because of their high electron conductivity, chemical stability, and inertness to both CO₂ reduction and HER catalytic reactions.³⁰ TM atoms can be trapped in the naturally or chemically formed defects of the graphene such as single vacancies (SVs) and double vacancies (DVs), presenting distinctively different properties from bulk metal materials.^{31–33} The introduction of N dopants can generate graphene defects that could significantly increase the concentration of TM atoms coordinated within the layers.³⁴ Although some previous studies suggested CO₂-to-CO catalysis on M-N-C sites, there was no direct evidence to demonstrate the single-atom morphology or the coordination environment of the active sites.^{35,36} Here, we report graphene shells (GSs) with Ni atoms embedded as a highly active electrocatalyst for CO₂ reduction to CO in an aqueous electrolyte. We employed three-dimensional (3D) atom probe tomography (APT) to directly identify the single Ni atomic sites in graphene vacancies. With density functional theory (DFT) calculations, we show that, compared with metallic Ni, Ni atomic sites in graphene can dramatically lower the CO₂ activation barrier, weaken the binding with CO for facile product release, and suppress the proton reduction side reaction. As a result, the catalyst exhibits a high faradic efficiency (FE) of ~93.2% toward CO formation under a significant current of ~20 mA/mg, which represents a turnover frequency (TOF) of ~8 s⁻¹ for the active Ni center, and can be further improved with a gas diffusion layer electrode in a flow cell.

RESULTS

The catalysts were synthesized by electrospinning of polymer nanofibers (NFs) with Ni and N precursors homogeneously distributed (*Supplemental Experimental Procedures*). Graphitized carbon NFs (CNFs, ~200 nm in diameter) catalyzed by uniformly dispersed Ni nanoparticles (NPs) (~20 nm in diameter) were obtained after the carbonization process of polymers (*Figures 1A* and *1B*).^{37–39} Carbon atoms alloyed with Ni under high temperature precipitated out and were catalyzed to form graphene layers on the Ni metal surface during the cooling down process. A closer observation of the Ni NPs by aberration-corrected scanning transmission electron microscopy (STEM) in *Figure 1C* reveals that the NP is tightly encapsulated by a few layers (~10 nm) of graphene, as confirmed by the averaged layer spacing of ~0.34 nm (NiN-GS; *Figure S1*). No Ni clusters were observed within the GS. This shell prevents the Ni NP from direct contact with the aqueous electrolyte and can thus dramatically suppress HER. The existence of Ni atoms in the surface shell was confirmed by energy-dispersive X-ray spectroscopy (EDS) mapping in *Figure 1D* (*Figure S2* and *Supplemental Experimental Procedures*). The Z-contrast STEM image on the left shows three bright areas representing three Ni NPs, with one of them highlighted by the yellow circle. In the Ni mapping image (marked by green dots), in addition to the NP regions with concentrated signals, Ni peaks were also detected in the neighboring carbon areas (*Figure S2*), demonstrating the successful incorporation of Ni atoms in the GS. N doping here plays a critical role in

¹Rowland Institute, Harvard University, Cambridge, MA 02142, USA

²SUNCAT Center for Interface Science and Catalysis, Department of Chemical Engineering, Stanford University, Stanford, CA 94305, USA

³Center for Nanoscale Systems, Harvard University, Cambridge, MA, USA

⁴Department of Materials Science and Engineering, Stanford University, Stanford, CA 94305, USA

⁵Department of Chemistry and Chemical Biology, Harvard University, Cambridge, MA 02138, USA

⁶Canadian Light Source Inc., University of Saskatchewan, 44 Innovation Boulevard, Saskatoon, SK S7N 2V3, Canada

⁷Shanghai Key Laboratory of Molecular Catalysis and Innovative Materials, Collaborative Innovation Center of Chemistry for Energy Materials, Department of Chemistry, Fudan University, Shanghai 200433, China

⁸School of Engineering and Applied Sciences, Harvard University, Cambridge, MA 02142, USA

⁹SUNCAT Center for Interface Science and Catalysis, SLAC National Accelerator Laboratory, 2575 Sand Hill Road, Menlo Park, CA 94025, USA

¹⁰Stanford Institute for Materials and Energy Sciences, SLAC National Accelerator Laboratory, 2575 Sand Hill Road, Menlo Park, CA 94025, USA

¹¹These authors contributed equally

¹²Lead Contact

*Correspondence: hwang@rowland.harvard.edu
<https://doi.org/10.1016/j.chempr.2017.09.014>

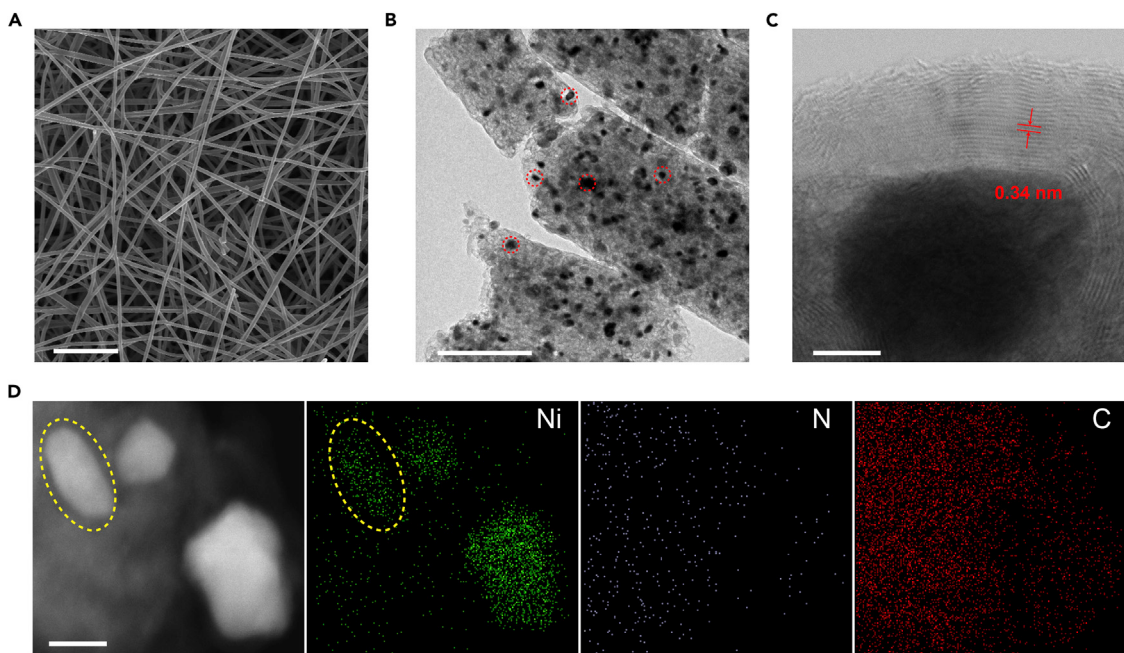


Figure 1. Characterizations of NiN-GS Catalysts

(A) Scanning electron microscopy (SEM) image of carbonized electrospun polymer NFs. Scale bar, 5 μm .

(B) TEM image of a ball-milled NiN-GS catalyst. The dark dots (highlighted by red circles as examples) uniformly distributed in the CNF are Ni NPs. Scale bar, 200 nm.

(C) Aberration-corrected STEM image of a Ni NP tightly wrapped by a few graphene layers. The Ni NP is \sim 20 nm in diameter. The GS is \sim 10 nm thick. The layer spacing is measured to be 0.34 nm. Scale bar, 5 nm.

(D) EDS mapping of the NiN-GS catalyst. Three Ni NPs were observed in the STEM image on the left, which is consistent with the Ni mapping image, with one of the NPs indicated by the yellow circle. Ni signals were detected in areas away from the NPs, demonstrating the successful incorporation of Ni atoms in graphene layers. The selected area spectra are shown in Figures S2 and S5. Scale bar, 20 nm.

creating defects in the graphene layers, which helps to trap and bond a significant number of Ni atoms in the GS.³⁴ This is demonstrated by both Raman and transmission electron microscopy (TEM) characterizations where the graphene layers in NiN-GS present a defective nature compared with the sample without N incorporation (Ni-GS; Figures S3 and S4 and *Supplemental Experimental Procedures*).⁴⁰ In addition, no Ni signals were detected in the GS outside the Ni NP in Ni-GS, because of the high quality of graphene synthesized (Figure S5). Those coordinated Ni atoms within the graphene layers in NiN-GS showed distinctively different oxidation states from Ni NPs covered below by X-ray photoelectron spectroscopy (XPS; Figure S6), suggesting the successful tuning of Ni electronic structures and thus the possible tuning of its catalytic activities.

The electrocatalytic CO₂RR performance of the NiN-GS catalyst, drop casted on a glassy carbon current collector, was performed in 0.1 M potassium bicarbonate (KHCO₃) electrolyte in a customized H cell (*Supplemental Experimental Procedures*). The different cyclic voltammograms (CVs) in CO₂ and N₂ saturated electrolyte suggest that reactions other than HER occur when CO₂ is present (Figures 2A and S7). Gas products were analyzed by gas chromatography (GC) at potential steps of 100 mV and further zoomed into 50 mV around the FE peak (Figures 2B and S8 and *Supplemental Experimental Procedures*). Detectable CO signals start at -0.35 V versus reversible hydrogen electrode (RHE), suggesting the onset overpotential of CO₂ to CO to be less than 230 mV (Figure S9). As the potential goes more negative, the FE of CO increases as the HER decreases (Figure 2B). The overall FE under different potentials ranges from 91.2% to 105.8% (Figures 2B, Table S1).

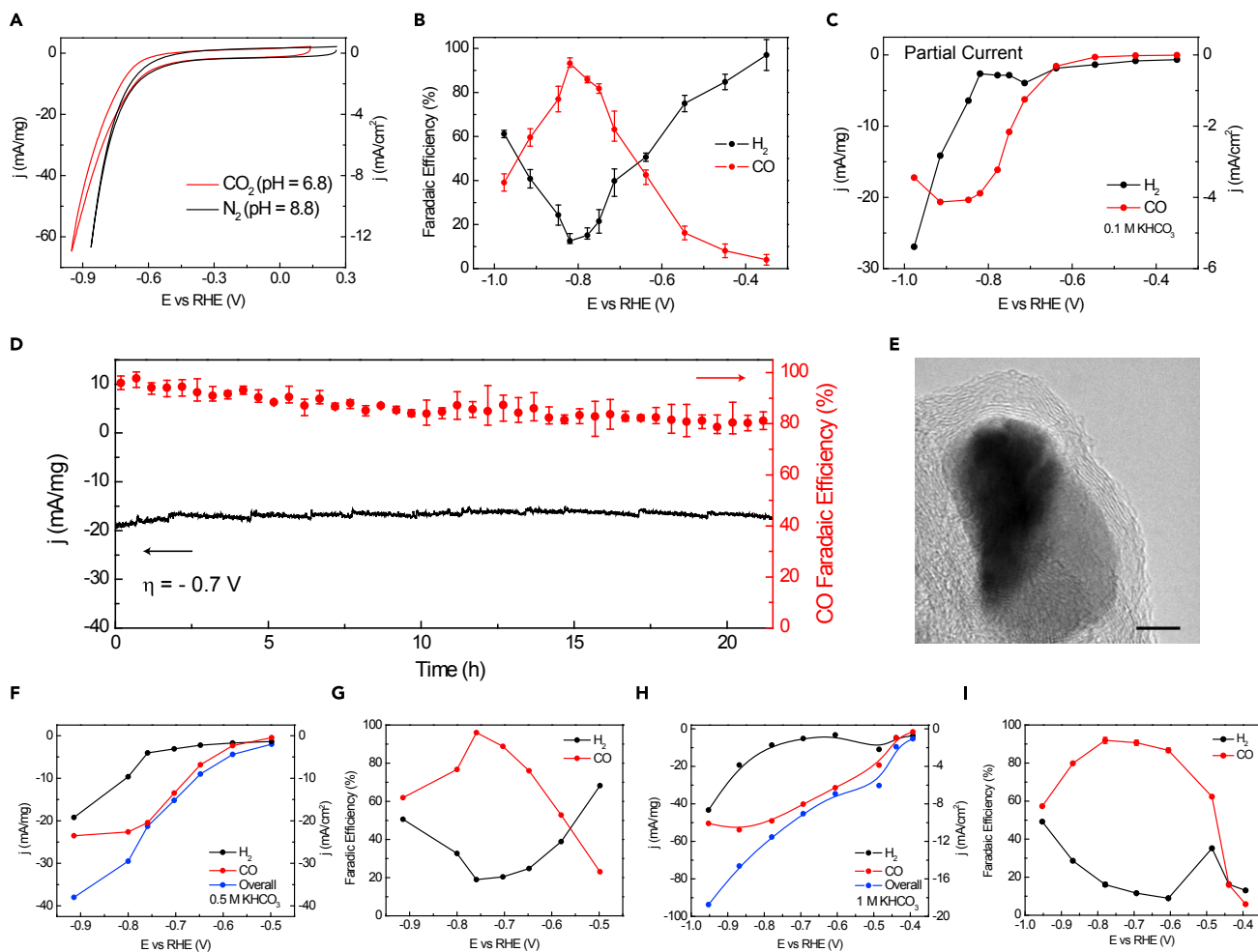


Figure 2. Electrocatalytic CO_2 Reduction Performance of NiN-GS

(A) CVs of NiN-GS in CO_2 and N_2 saturated electrolyte, suggesting a different reaction pathway when CO_2 is present.

(B) FEs of H_2 and CO under different applied potentials for NiN-GS. The error bars are based on three identical samples. The highest CO FE is 93.2% under -0.82 V versus RHE, with an overpotential of -0.7 V . The error bars represent three identical samples.

(C) Partial currents of H_2 and CO. The CO evolution current density is around 20 mA/mg under the highest CO FE.

(D) Long-term electrolysis test under -0.7 V overpotential. The high FE of CO is maintained for more than 20 hr, suggesting good stability of the NiN-GS catalyst. The error bars represent three identical samples.

(E) The TEM image of post-catalysis NiN-GS. Scale bar, 5 nm.

(F and G) CO_2RR catalytic performance (current densities in F and FEs in G) of 1 mg/cm² NiN-GS catalyst on a high-surface-area CFP electrode in 0.5 M KHCO_3 electrolyte.

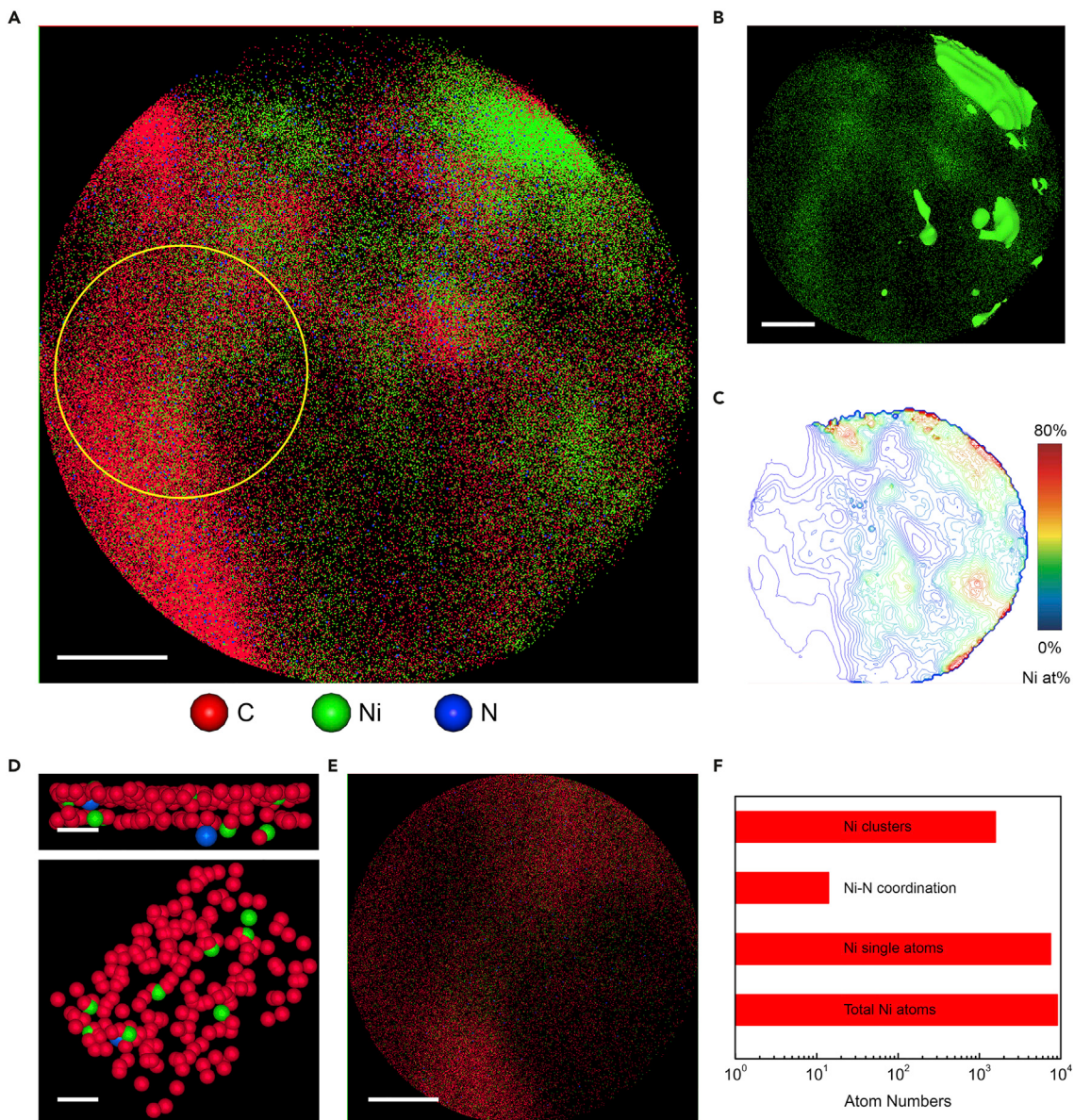
(H and I) CO_2RR performance (current densities in H and FEs in I) of NiN-GS catalyst on a gas diffusion layer electrode in a flow cell configuration. The catalyst mass loading is the same as for glassy carbon electrode in (A)–(D).

The highest FE of CO_2 to CO reaches 93.2% at 0.7 V overpotential, with a CO evolution current density of $\sim 20 \text{ mA/mg}$ (4 mA/cm^2 at $0.2 \text{ mg}/\text{cm}^2$ mass loading; Figures 2C and S10). An isotope $^{13}\text{CO}_2$ labeling experiment was performed on GC-mass spectroscopy to confirm that the gas product of CO comes from CO_2 reduction (Figure S11 and Supplemental Experimental Procedures). The Tafel slope plotted with electrolysis currents and overpotentials was 138.5 mV/decade (Figure S12).^{9,40–42} No other gas or liquid products were detected by GC or ^1H NMR (Figure S13). Whether these surrounded GSs will be stable under long-term operations is a concern, because if the protection layer breaks, the Ni NPs will be exposed to water and could produce H_2 heavily.¹⁹ Around 80% FE of CO was

still maintained after more than 20 hr of continuous electrolysis under 0.7 V overpotential (Figure 2D), suggesting the excellent stability of the catalytic sites. A post-catalysis TEM examination also confirmed that the core-shell structure remains intact to prevent contact between Ni NPs and water (Figures 2E and S14). The CO₂RR geometrical current density can be significantly improved to more than 20 mA/cm² by loading more NiN-GS catalysts onto high-surface-area carbon fiber paper (CFP) substrate while maintaining high CO FEs in 0.5 M KHCO₃ electrolyte (Figures 2F and 2G). In addition, the overpotential can be further improved by applying NiN-GS catalyst (0.2 mg/cm²) onto a gas diffusion layer electrode in a flow cell (Figures 2H and 2I),⁴³ where a CO partial current of 31.4 mA/mg was obtained at 0.48 V overpotential (Supplemental Experimental Procedures, Figure S15, and Tables S1 and S2).

Control experiments were performed to provide important clues on the possible active sites in NiN-GS for this highly selective CO₂ reduction. First, it is unlikely that the Ni NP cores are in contact with the electrolyte to participate in the gas reduction reactions. This is confirmed by the TEM images of NiN-GS after an acid leaching process (AL-NiN-GS; Figure S16 and Supplemental Experimental Procedures),⁴⁴ which show the Ni NPs to be well protected from concentrated protons by the tightly surrounded GSs. Only by violent ball milling followed by acid leaching can we break off some core-shell structures and allow acids to attack Ni NPs (VAL-NiN-GS; Figure S16 and Supplemental Experimental Procedures). In addition, Ni-GS with Ni NPs embedded presents nearly no activity toward CO formation (Figures S17 and S18). Second, the dramatically decreased CO evolution activity per electrochemical surface area (Figure S19) after acid leaching processes suggest that Ni atoms in the surface GS play a more important role than the N dopants (Figure S20).^{36,40,41} Third, Co and Fe catalysts with the same core-shell structure and N doping (Figure S21 and Supplemental Experimental Procedures), however, present lower activity and selectivity toward CO formation than NiN-GS (Figure S22), indicating that the high CO FE is related to the specific electronic structure of Ni sites in the GS.

More detailed characterizations to elucidate the nature of Ni atomic sites in graphene layers become important for a clear understanding of the catalytic active sites. Here, we used APT technology (Figure S23) to reveal^{45,46} whether the Ni atoms are isolated single atoms or small clusters and whether the Ni atomic sites are coordinated with N or not. The 3D tomography of NiN-GS catalyst is presented in Movie S1, and the projected 2D image is shown in Figure 3A. Each pixel represents one single atom. As shown in Figure 3B and Movie S2, away from the areas with concentrated Ni (Ni NPs), there are also a significant number of Ni atoms dispersed in carbon, consistent with our EDX mapping in Figure 1D. The contour map with an interval of 2 at % in Figure 3C provides detailed distribution information on Ni atoms in the catalyst, with decreased Ni atom concentrations away from the Ni sources. The local coordination environment of the Ni atoms is shown by taking a closer look at the graphene layers in Figure 3D. There are a few Ni single atoms coordinated in graphene vacancies, providing direct evidence of the single Ni atomic site. No Ni clusters were observed. In addition, we also noticed that there is one Ni atom coordinated with one N atom in a graphene vacancy, suggesting a small ratio of Ni atomic sites coordinated with N atoms. More detailed information about the surrounding coordination of Ni atomic sites can be extracted from statistics and quantitative analysis (Figure 3F). The selected area with dispersed Ni atoms is indicated by the yellow circle in Figure 3A and enlarged in Figure 3E. Among all the Ni atoms in this area, 83% are single atoms, without neighboring Ni atoms closer than 2.2 Å (Figure S24). In addition, in those Ni single atoms, only 0.2% of them are directly coordinated with one neighboring N (less than 2 Å), suggesting that most of the Ni atomic sites are coordinated with C atoms. Single-atom

**Figure 3. ATP of the NiN-GS Catalyst**

- (A) The 2D atom map of NiN-GS. The yellow circle represents the selected area for statistical studies in (E) and (F). Scale bar, 10 nm.
- (B) The 2D projected view of Ni atoms. The green areas represent Ni-rich areas (>50 at %). Away from the Ni sources, there are still a significant number of Ni atoms dispersed in the carbon area. Scale bar, 10 nm.
- (C) The contour map of Ni concentration with an interval of 2 at %.
- (D) Zoomed in side view (upper) and top view (lower) of graphene layers with Ni single atoms coordinated in vacancies. Only one Ni atom is directly coordinated with one N atom. Scale bars, 1 nm.
- (E) Atom map of the selected area in (A) as indicated by the yellow circle. Scale bar, 5 nm.
- (F) The statistics of the selected area in (E). Most of the Ni atoms are in single-atom morphology, and 0.2% of them are coordinated with N atoms.

coordination in the graphene shell is also observed by X-ray absorption spectroscopy as the small peak at ~ 1.4 Å in R space beside the dominating Ni–Ni bonding signal from those embedded Ni NPs (Supplemental Experimental Procedures and Figure S24). In addition, the *in situ* electrochemical attenuated total reflection infrared spectroscopy (ATR-IR) result with adsorbed monolayer CO as a surface probe further demonstrates the single Ni atomic sites on the surface of the NiN-GS catalyst

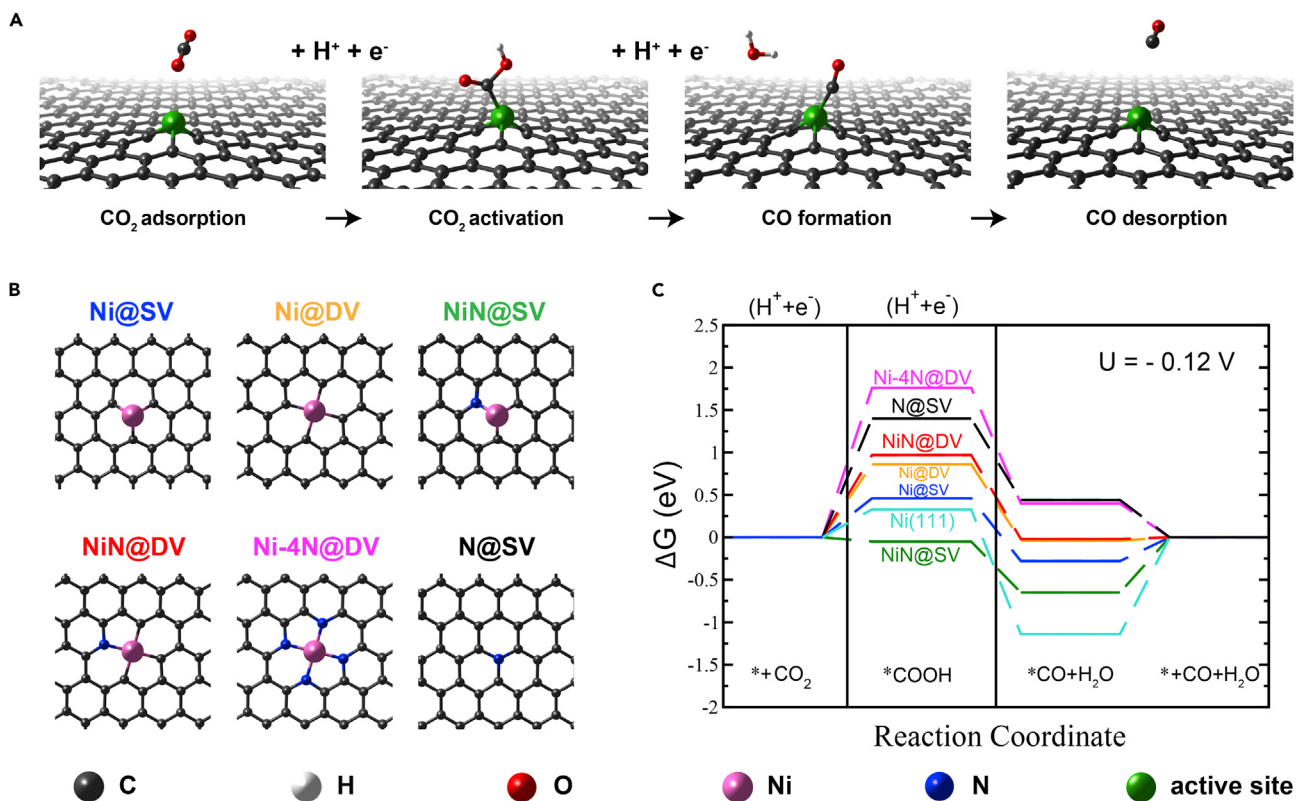


Figure 4. Simulations of CO_2 -to-CO Reduction on Different Atomic Sites

(A) Schematic of the reaction steps of electrocatalytic CO_2 to CO reduction.

(B) Different atomic configurations in graphene for the DFT calculations.

(C) The free energy diagram of CO_2 to CO conversion on different atomic sites under an equilibrium potential of -0.12 V versus RHE.

(Figure S25).^{24,47} Therefore, we believe that the Ni sites in GS should be the active centers for electrocatalytic CO_2 to CO conversion, which exhibits a high TOF of $\sim 8 \text{ s}^{-1}$ and a cumulative turnover number (TON) of up to 454,000 under -0.7 V overpotential during 20 hr of continuous electrolysis (Figure S26 and *Supplemental Experimental Procedures*).

DISCUSSION

To further investigate the origin of the activity of the NiN-GS catalyst, we studied the reaction steps involved in the CO_2 to CO electrocatalytic reduction by using DFT calculations (Figure 4A). We considered Ni atoms trapped in single or double vacancies (Ni@SV and Ni@DV, respectively) of the graphene sheet, with a variety of possible N coordination to Ni sites as well as N dopants (N@SV) (Figure S27 and *Supplemental Experimental Procedures*), among which the most stable and active structures are shown in Figure 4B (Table S3). A simple thermochemical analysis shows that the pathway for CO_2 reduction to CO goes through $*\text{COOH}$ and $*\text{CO}$ intermediates (Figures 4A).^{48–50} The solvation correction is included in Figure S28 (*Supplemental Experimental Procedures*). The free energy diagram for each reaction step on different atomic structures, including the Ni (111) surface, was calculated at the equilibrium potential (-0.12 V versus RHE) in Figure 4C, where CO_2 activation ($*\text{COOH}$ formation) or CO desorption are suggested to be the rate-limiting steps on different sites. As an example, on Ni (111) metal surface, even though the $*\text{COOH}$ formation is facile, the binding with CO is too strong as indicated by the deep thermodynamic sink

(−1.14 eV) in Figure 4C, which dramatically limits the CO desorption process and thus the overall catalytic performance. This is consistent with the observation that Ni metal evolves primarily H₂ under CO₂ reduction conditions.¹⁸ However, when Ni atoms are coordinated in graphene layers, the electronic structure is drastically changed, exhibiting a much higher projected density of states around Fermi energy than that of Ni (111) (Figures S6 and S29). As a result, the binding with CO is significantly weakened for a facile CO desorption (Figure 4C and Table S4). In addition, compared with N dopants in graphene, the Ni atomic sites such as Ni@SV and NiN@SV present decreased *COOH formation energies (Figure 4C and Table S4).²¹ Direct coordination of N to Ni atoms in graphene layers helps to pull the electrons away from Ni, which as a result makes the *COOH formation thermodynamically downhill on NiN@SV. However, it binds CO slightly more strongly than Ni@SV (Table S4). Combined with APT characterizations, this analysis therefore suggests that the Ni atoms coordinated in the graphene vacancies, such as Ni@SV and Ni@DV, are the major active sites for electrocatalytic CO₂ reduction to CO, where N atoms play a critical role in generating defects in graphene to trap Ni atoms. The minority atomic sites in this catalyst system, such as NiN@SV or NiN@DV, could also be highly active for CO₂RR as suggested by the DFT simulations. The calculated H-binding energy, a good descriptor for HER activity,^{51–53} suggests significantly suppressed hydrogen generation on Ni@SV, Ni@DV, and NiN@SV sites ($\Delta G_H = 0.50, 0.56$, and 0.52 eV, respectively) in comparison with Ni (111) metal surface ($\Delta G_H = -0.26$ eV),^{52,53} which is consistent with our experimental results (Table S5). The CO₂RR selectivity of different active sites can be further evaluated by the difference between the thermodynamic limiting potentials for CO₂ reduction and HER, $U_L(\text{CO}_2) - U_L(\text{H}_2)$, which confirms the high selectivity of both Ni@SV and Ni@DV (Figure S30). Because of the different electronic structures, Co atomic sites present stronger CO binding and higher HER catalytic activity than Ni sites (Table S6), which explains its lower CO selectivity (Figure S22).

For a practical electrosynthetic cell of CO₂ reduction to fuels, an active and stable oxygen evolution reaction (OER) catalyst needs to be paired to efficiently oxidize water and free the protons.^{10,54} Different from previous literature where CO₂RR and OER catalysts were usually separated by a bipolar membrane and operated in different pH solutions,^{55,56} here we developed the Li⁺-tuned Co₃O₄ NPs as an active and stable OER catalyst in neutral pH to be coupled with NiN-GS for a pH-equal (pH 7.5) electrolysis system (Figures S31–S35 and Supplemental Experimental Procedures).²⁰ Powered by a single cell of commercialized GaInP₂/GaAs/Ge TJ photovoltaic, our artificial photosynthesis system delivers a peak solar-to-CO efficiency of 12.7% (Figures S36 and S37). Incorporating TM atoms into a well-defined 2D matrix can effectively tune their electronic structures and thus favor the desired reaction pathways. Given the wide variety of 2D layered materials, which provide different types of chemical environments for tuning different TM atoms, this approach creates an important platform for designing active CO₂ reduction catalysts with high selectivity toward CO and higher-value hydrocarbons, which is of great importance to both technological applications in renewable energies and fundamental mechanism studies in catalysis.

EXPERIMENTAL PROCEDURES

The NiN-GS catalyst was first prepared by electrospinning a precursor solution containing polyacrylonitrile ($M_w = 150,000$), polypyrrolidone ($M_w = 1,300,000$), Ni(NO₃)₂ 6H₂O, dicyandiamide, and dimethylformamide, followed by a polymer nanofiber oxidation and a carbonization procedure (Supplemental Experimental Procedures). The as-synthesized NiN-GS catalyst was ball milled for 5 min to nanopowder for catalysis and characterization.

The STEM characterization in [Figure 1C](#) and other EDS analysis were carried out with a JEOL ARM200F aberration-corrected scanning transmission electron microscope. All other TEM images were obtained with a JEOL 2100 TEM. Specimens for 3D APT were prepared with an FEI Helios 660 Nanolab Dual-Beam FIB/SEM. APT was then performed with a Cameca LEAP 4000 HR operated in laser mode. Approximately 2.3 million atoms were collected in the dataset presented. The data were reconstructed and analyzed with Cameca's IVAS software according to standard reconstruction protocols.

In situ electrochemical ATR-IR measurements were run on a catalyst layer covered hemicylindrical Si prism with a Nicolet iS50 FTIR spectrometer. Raman spectroscopy was carried out on a WITEC CRM200 confocal Raman spectrometer with a 532 nm laser source. XPS was obtained with a Thermo Scientific K-Alpha ESCA spectrometer, and the surface componental content and peak fitting was analyzed with the Thermo Avantage V5 program for selected elemental scans. The Ni K-edge XAS was acquired in fluorescence mode with the SXRMB beamline of Canadian Light Source. Powder XRD data were collected with a Bruker D2 Phaser diffractometer.

The electrochemical measurements were run at 25°C in a customized gas-tight H cell ([Figure S8](#)) or flow cell ([Figure S15](#)) or a 3D-printed electrosynthetic cell ([Figure S35](#)) separated by Nafion 117 membrane. A BioLogic VMP3 workstation was used to record the electrochemical response. All measured potentials in this work were converted to the RHE scale with manual *iR* compensation. During electrolysis, CO₂ gas was delivered into the cathodic compartment containing CO₂-saturated KHCO₃ electrolyte and vented into a Shimadzu GC-2014 gas chromatograph equipped with a thermal conductivity detector and a flame ionization detector coupled with a methanizer.

All other experimental and setup details, as well the DFT calculations, are provided in the [Supplemental Experimental Procedures](#).

SUPPLEMENTAL INFORMATION

Supplemental Information includes Supplemental Experimental Procedures, 37 figures, 6 tables, and 2 movies and can be found with this article online at <https://doi.org/10.1016/j.chempr.2017.09.014>.

AUTHOR CONTRIBUTIONS

H.W. conceived the project. H.W. and K.J. synthesized materials and measured catalysts. H.W., K.J., A.J.A., Y.L., Z.L., J.L., Y.H., and Y.Z. characterized materials. S.S., K.C., and J.K.N. performed simulations. All authors analyzed the results. H.W., K.J., and S.S. wrote the manuscript. H.W. supervised the project.

ACKNOWLEDGMENTS

This work was supported by the Rowland Fellows Program at the Rowland Institute of Harvard University. H.W. and K.J. acknowledge great support from the Friend group at Harvard University. S.S., Y.L., Z.L., J.K.N., and Y.C. acknowledge support from the Global Climate and Energy Project at Stanford University. K.C. and J.K.N. acknowledge support from the Joint Center for Artificial Photosynthesis, a DOE Energy Innovation Hub, supported through the Office of Science of the US Department of Energy under award number DESC0004993. W.B.C. and Y.Z. acknowledge support from the 973 Program of the Chinese Ministry of Science and Technology (2015CB932303) and Natural Science Foundation of China (21733004 and 21327901). This work was performed in part at the Center for Nanoscale Systems

(CNS), a member of the National Nanotechnology Infrastructure Network, which is supported by the National Science Foundation under award no. ECS-0335765. The CNS is part of Harvard University. We acknowledge great support from Spectrolab for the triple-junction solar cell used in this work. We acknowledge the Nocera group at Harvard University for helping with the solar simulator. We acknowledge the helpful discussion on flow cells with Prof. Kenis and Mr. Sumit at the University of Illinois at Urbana-Champaign.

Received: August 1, 2017

Revised: September 15, 2017

Accepted: September 26, 2017

Published: October 19, 2017

REFERENCES AND NOTES

- Cook, T.R., Dogutan, D.K., Reece, S.Y., Surendranath, Y., Teets, T.S., and Nocera, D.G. (2010). Solar energy supply and storage for the legacy and nonlegacy worlds. *Chem. Rev.* 110, 6474–6502.
- Meyer, T.J. (1989). Chemical approaches to artificial photosynthesis. *Acc. Chem. Res.* 22, 163–170.
- Sakimoto, K.K., Wong, A.B., and Yang, P. (2016). Self-photosensitization of nonphotosynthetic bacteria for solar-to-chemical production. *Science* 351, 74–77.
- Liu, C., Colón, B.C., Ziesack, M., Silver, P.A., and Nocera, D.G. (2016). Water splitting–biosynthetic system with CO₂ reduction efficiencies exceeding photosynthesis. *Science* 352, 1210–1213.
- Lewis, N.S., and Nocera, D.G. (2006). Powering the planet: chemical challenges in solar energy utilization. *Proc. Natl. Acad. Sci. USA* 103, 15729–15735.
- Jhong, H.-R.M., Ma, S., and Kenis, P.J.A. (2013). Electrochemical conversion of CO₂ to useful chemicals: current status, remaining challenges, and future opportunities. *Curr. Opin. Chem. Eng.* 2, 191–199.
- Li, C.W., Ciston, J., and Kanan, M.W. (2014). Electrocatalysis of carbon monoxide to liquid fuel on oxide-derived nanocrystalline copper. *Nature* 508, 504–507.
- Gao, S., Lin, Y., Jiao, X., Sun, Y., Luo, Q., Zhang, W., Li, D., Yang, J., and Xie, Y. (2016). Partially oxidized atomic cobalt layers for carbon dioxide electroreduction to liquid fuel. *Nature* 529, 68–71.
- Lin, S., Diercks, C.S., Zhang, Y.-B., Kornienko, N., Nichols, E.M., Zhao, Y., Paris, A.R., Kim, D., Yang, P., Yaghi, O.M., et al. (2015). Covalent organic frameworks comprising cobalt porphyrins for catalytic CO₂ reduction in water. *Science* 349, 1208–1213.
- Asadi, M., Kim, K., Liu, C., Addepalli, A.V., Abbas, P., Yasaei, P., Phillips, P., Behranginia, A., Cerrato, J.M., Haasch, R., et al. (2016). Nanostructured transition metal dichalcogenide electrocatalysts for CO₂ reduction in ionic liquid. *Science* 353, 467–470.
- Rosen, B.A., Salehi-Khojin, A., Thorson, M.R., Zhu, W., Whipple, D.T., Kenis, P.J.A., and
- Masel, R.I. (2011). Ionic liquid-mediated selective conversion of CO₂ to CO at low overpotentials. *Science* 334, 643–644.
- Costentin, C., Robert, M., and Savéant, J.-M. (2013). Catalysis of the electrochemical reduction of carbon dioxide. *Chem. Soc. Rev.* 42, 2423–2436.
- Bligaard, T., Nørskov, J.K., Dahl, S., Matthesen, J., Christensen, C.H., and Sehested, J. (2004). The Brønsted–Evans–Polanyi relation and the volcano curve in heterogeneous catalysis. *J. Catal.* 224, 206–217.
- Zhu, W., Michalsky, R., Metin, Ö., Lv, H., Guo, S., Wright, C.J., Sun, X., Peterson, A.A., and Sun, S. (2013). Monodisperse Au nanoparticles for selective electrocatalytic reduction of CO₂ to CO. *J. Am. Chem. Soc.* 135, 16833–16836.
- Liu, M., Pang, Y., Zhang, B., De Luna, P., Voznyy, O., Xu, J., Zheng, X., Dinh, C.T., Fan, F., Cao, C., et al. (2016). Enhanced electrocatalytic CO₂ reduction via field-induced reagent concentration. *Nature* 537, 382–386.
- Chen, Y., Li, C.W., and Kanan, M.W. (2012). Aqueous CO₂ reduction at very low overpotential on oxide-derived Au nanoparticles. *J. Am. Chem. Soc.* 134, 19969–19972.
- Kuhl, K.P., Hatsukade, T., Cave, E.R., Abram, D.N., Kibsgaard, J., and Jaramillo, T.F. (2014). Electrocatalytic conversion of carbon dioxide to methane and methanol on transition metal surfaces. *J. Am. Chem. Soc.* 136, 14107–14113.
- Hori, Y., Wakebe, H., Tsukamoto, T., and Koga, O. (1994). Electrocatalytic process of CO selectivity in electrochemical reduction of CO₂ at metal electrodes in aqueous media. *Electrochim. Acta* 39, 1833–1839.
- Gong, M., Zhou, W., Tsai, M.-C., Zhou, J., Guan, M., Lin, M.-C., Zhang, B., Hu, Y., Wang, D.-Y., Yang, J., et al. (2014). Nanoscale nickel oxide/nickel heterostructures for active hydrogen evolution electrocatalysis. *Nat. Commun.* 5, 4695.
- Wang, H., Lee, H.-W., Deng, Y., Lu, Z., Hsu, P.-C., Liu, Y., Lin, D., and Cui, Y. (2015). Bifunctional non-noble metal oxide nanoparticle electrocatalysts through lithium-induced conversion for overall water splitting. *Nat. Commun.* 6, 7261.
- Shi, C., Hansen, H.A., Lausche, A.C., and Nørskov, J.K. (2014). Trends in electrochemical CO₂ reduction activity for open and close-packed metal surfaces. *Phys. Chem. Chem. Phys.* 16, 4720–4727.
- Chen, Y., and Kanan, M.W. (2012). Tin oxide dependence of the CO₂ reduction efficiency on tin electrodes and enhanced activity for tin/tin oxide thin-film catalysts. *J. Am. Chem. Soc.* 134, 1986–1989.
- Kim, D., Resasco, J., Yu, Y., Asiri, A.M., and Yang, P. (2014). Synergistic geometric and electronic effects for electrochemical reduction of carbon dioxide using gold–copper bimetallic nanoparticles. *Nat. Commun.* 5, 4948.
- Jiang, K., Wang, H., Cai, W.-B., and Wang, H. (2017). Li electrochemical tuning of metal oxide for highly selective CO₂ reduction. *ACS Nano* 11, 6451–6458.
- Nishihara, H., Hirota, T., Matsuura, K., Ohwada, M., Hoshino, N., Akutagawa, T., Higuchi, T., Jinsei, H., Koseki, Y., Kasai, H., et al. (2017). Synthesis of ordered carbonaceous frameworks from organic crystals. *Nat. Commun.* 8, 109.
- Manthiram, K., Beberwyck, B.J., and Alivisatos, A.P. (2014). Enhanced electrochemical methanation of carbon dioxide with a dispersible nanoscale copper catalyst. *J. Am. Chem. Soc.* 136, 13319–13325.
- Lei, F., Liu, W., Sun, Y., Xu, J., Liu, K., Liang, L., Yao, T., Pan, B., Wei, S., and Xie, Y. (2016). Metallic tin quantum sheets confined in graphene toward high-efficiency carbon dioxide electroreduction. *Nat. Commun.* 7, 12697.
- Yang, M., Li, S., Wang, Y., Herron, J.A., Xu, Y., Allard, L.F., Lee, S., Huang, J., Mavrikakis, M., and Flytzani-Stephanopoulos, M. (2014). Catalytically active Au-O(OH)_x-species stabilized by alkali ions on zeolites and mesoporous oxides. *Science* 346, 1498–1501.
- Manthiram, K., Surendranath, Y., and Alivisatos, A.P. (2014). Dendritic assembly of gold nanoparticles during fuel-forming electrocatalysis. *J. Am. Chem. Soc.* 136, 7237–7240.
- Novoselov, K.S., Geim, A.K., Morozov, S.V., Jiang, D., Zhang, Y., Dubonos, S.V., Grigorieva,

- I.V., and Firsov, A.A. (2004). Electric field effect in atomically thin carbon films. *Science* 306, 666–669.
31. Rodríguez-Manzo, J.A., Cretu, O., and Banhart, F. (2010). Trapping of metal atoms in vacancies of carbon nanotubes and graphene. *ACS Nano* 4, 3422–3428.
32. Giovanni, M., Poh, H.L., Ambrosi, A., Zhao, G., Sofer, Z., Sanek, F., Khezri, B., Webster, R.D., and Pumera, M. (2012). Noble metal (Pd, Ru, Rh, Pt, Au, Ag) doped graphene hybrids for electrocatalysis. *Nanoscale* 4, 5002–5008.
33. Krasheninnikov, A.V., Lehtinen, P.O., Foster, A.S., Pyykkö, P., and Nieminen, R.M. (2009). Embedding transition-metal atoms in graphene: structure, bonding, and magnetism. *Phys. Rev. Lett.* 102, 126807.
34. Li, Y., Zhou, W., Wang, H., Xie, L., Liang, Y., Wei, F., Idrobo, J.-C., Pennycook, S.J., and Dai, H. (2012). An oxygen reduction electrocatalyst based on carbon nanotube-graphene complexes. *Nat. Nanotech.* 7, 394–400.
35. Su, P., Iwase, K., Nakanishi, S., Hashimoto, K., and Kamiya, K. (2016). Nickel-nitrogen-modified graphene: an efficient electrocatalyst for the reduction of carbon dioxide to carbon monoxide. *Small* 12, 6083–6089.
36. Varela, A.S., Ranjbar Sahraie, N., Steinberg, J., Ju, W., Oh, H.-S., and Strasser, P. (2015). Metal-doped nitrogenated carbon as an efficient catalyst for direct CO₂ electroreduction to CO and hydrocarbons. *Angew. Chem. Int. Ed.* 54, 10758–10762.
37. Chen, Z., Ren, W., Gao, L., Liu, B., Pei, S., and Cheng, H.-M. (2011). Three-dimensional flexible and conductive interconnected graphene networks grown by chemical vapour deposition. *Nat. Mater.* 10, 424–428.
38. Deng, D., Novoselov, K.S., Fu, Q., Zheng, N., Tian, Z., and Bao, X. (2016). Catalysis with two-dimensional materials and their heterostructures. *Nat. Nanotech.* 11, 218–230.
39. Kumar, B., Asadi, M., Pisasale, D., Sinha-Ray, S., Rosen, B.A., Haasch, R., Abiade, J., Yarin, A.L., and Salehi-Khojin, A. (2013). Renewable and metal-free carbon nanofibre catalysts for carbon dioxide reduction. *Nat. Commun.* 4, 2819.
40. Sharma, P.P., Wu, J., Yadav, R.M., Liu, M., Wright, C.J., Tiwary, C.S., Yakobson, B.I., Lou, J., Ajayan, P.M., and Zhou, X.-D. (2015). Nitrogen-doped carbon nanotube arrays for high-efficiency electrochemical reduction of CO₂: on the understanding of defects, defect density, and selectivity. *Angew. Chem. Int. Ed.* 54, 13701–13705.
41. Wu, J., Yadav, R.M., Liu, M., Sharma, P.P., Tiwary, C.S., Ma, L., Zou, X., Zhou, X.-D., Yakobson, B.I., Lou, J., et al. (2015). Achieving highly efficient, selective, and stable CO₂ reduction on nitrogen-doped carbon nanotubes. *ACS Nano* 9, 5364–5371.
42. Kornienko, N., Zhao, Y., Kley, C.S., Zhu, C., Kim, D., Lin, S., Chang, C.J., Yaghi, O.M., and Yang, P. (2015). Metal-organic frameworks for electrocatalytic reduction of carbon dioxide. *J. Am. Chem. Soc.* 137, 14129–14135.
43. Jhong, H.-R.M., Brushett, F.R., and Kenis, P.J.A. (2013). The effects of catalyst layer deposition methodology on electrode performance. *Adv. Energy Mater.* 3, 589–599.
44. Zhao, Y., Nakamura, R., Kamiya, K., Nakanishi, S., and Hashimoto, K. (2013). Nitrogen-doped carbon nanomaterials as non-metal electrocatalysts for water oxidation. *Nat. Commun.* 4, 2390.
45. Tedsree, K., Li, T., Jones, S., Chan, C.W.A., Yu, K.M.K., Bagot, P.A.J., Marquis, E.A., Smith, G.D.W., and Tsang, S.C.E. (2011). Hydrogen production from formic acid decomposition at room temperature using a Ag-Pd core-shell nanocatalyst. *Nat. Nanotech.* 6, 302–307.
46. Kelly, T.F., and Miller, M.K. (2007). Atom probe tomography. *Rev. Sci. Instrum.* 78, 031101.
47. Huo, S.-J., Wang, J.-Y., Yao, J.-L., and Cai, W.-B. (2010). Exploring electrosorption at iron electrode with *in situ* surface-enhanced infrared absorption spectroscopy. *Anal. Chem.* 82, 5117–5124.
48. Hansen, H.A., Varley, J.B., Peterson, A.A., and Nørskov, J.K. (2013). Understanding trends in the electrocatalytic activity of metals and enzymes for CO₂ reduction to CO. *J. Phys. Chem. Lett.* 4, 388–392.
49. Hansen, H.A., Shi, C., Lausche, A.C., Peterson, A.A., and Nørskov, J.K. (2016). Bifunctional alloys for the electroreduction of CO₂ and CO. *Phys. Chem. Chem. Phys.* 18, 9194–9201.
50. Peterson, A.A., and Nørskov, J.K. (2012). Activity descriptors for CO₂ electroreduction to methane on transition-metal catalysts. *J. Phys. Chem. Lett.* 3, 251–258.
51. Hinnemann, B., Moses, P.G., Bonde, J., Jørgensen, K.P., Nielsen, J.H., Horch, S., Chorkendorff, I., and Nørskov, J.K. (2005). Biomimetic hydrogen evolution: MoS₂ nanoparticles as catalyst for hydrogen evolution. *J. Am. Chem. Soc.* 127, 5308–5309.
52. Greeley, J., Jaramillo, T.F., Bonde, J., Chorkendorff, I., and Nørskov, J.K. (2006). Computational high-throughput screening of electrocatalytic materials for hydrogen evolution. *Nat. Mater.* 5, 909–913.
53. Greeley, J., Nørskov, J.K., Kibler, L.A., El-Aziz, A.M., and Kolb, D.M. (2006). Hydrogen evolution over bimetallic systems: understanding the trends. *ChemPhysChem* 7, 1032–1035.
54. Schreier, M., Curvat, L., Giordano, F., Steier, L., Abate, A., Zakeeruddin, S.M., Luo, J., Mayer, M.T., and Grätzel, M. (2015). Efficient photosynthesis of carbon monoxide from CO₂ using perovskite photovoltaics. *Nat. Commun.* 6, 7326.
55. Schreier, M., Héroguel, F., Steier, L., Ahmad, S., Luterbacher, J.S., Mayer, M.T., Luo, J., and Grätzel, M. (2017). Solar conversion of CO₂ to CO using earth-abundant electrocatalysts prepared by atomic layer modification of CuO. *Nat. Energy* 2, 17087.
56. Zhou, X., Liu, R., Sun, K., Chen, Y., Verlage, E., Francis, S.A., Lewis, N.S., and Xiang, C. (2016). Solar-driven reduction of 1 atm of CO₂ to formate at 10% energy-conversion efficiency by use of a TiO₂-protected III-V tandem photoanode in conjunction with a bipolar membrane and a Pd/C Cathode. *ACS Energy Lett.* 1, 764–770.